ELSEVIER

Achieving superb strength in single-phase FCC alloys via maximizing volume misfit

Zhongtao Li [1], Shihua Ma [2], Shijun Zhao [2], Weidong Zhang [1], Fei Peng [1], Qian Li [3], Tao Yang [3], Chia-Yi Wu [4], Daixiu Wei [5], Yi-Chia Chou [6], Peter K. Liaw [7], Yanfei Gao [7], Zhenggang Wu [1]

[1] College of Materials Science and Engineering, Hunan University, Changsha 410082, China
[2] Department of Mechanical Engineering, City University of Hong Kong, Hong Kong, China
[3] Department of Materials Science and Engineering, City University of Hong Kong, Hong Kong, China
[4] Department of Electrophysics, National Yang Ming Chiao Tung University, Hsinchu 30010, Taiwan
[5] Institute for Materials Research, Tohoku University, 2-1-1 Katahira, Sendai, Miyagi 980-8577, Japan
[6] Department of Materials Science and Engineering, National Taiwan University, Taipei 10617, Taiwan
[7] Department of Materials Science and Engineering, The University of Tennessee, Knoxville, TN 37996-2100, USA

Single-phase face-centered cubic (SP-FCC) alloys normally possess low strength. Conventionally strengthening strategies inevitably cause significant ductility sacrifice. Here, a single-phase Ni-based FCC alloy with a superb yield strength of ~1.05GPa and a good ductility of 37% is designed through maximizing the volume misfits. The misfit of the purposely targeted $Ni_{80}Mo_{20}$ alloy is severer than all existing FCC alloys, bringing the alloy a highest-ever Hall-Petch coefficient (k_{HP} = 1034 MPa·μm$^{1/2}$) and a pronounced solid solution strengthening ($\Delta\sigma_{ss}$ = 224 MPa). Current work yields two surprising and novel findings for SP-FCC alloys. First, volume misfit is a good pertinent indicator of k_{HP}. Second, the conventional impression about the sole contribution of edge dislocations to strengthening in SP-FCC alloys may no longer hold; instead, screw dislocations can also kick in once the nonsphericity of the solute-induced stress field reaches a critical value. Altogether, this work paves a new avenue of pursuing ultimate strengthening without significant ductility sacrifice for SP-FCC alloys relying on the volume-misfit-maximization strategy.

Keywords: Single-phase face-centered cubic alloys; Volume misfit; Solid-solution strengthening; Grain-boundary strengthening; Mechanical properties

Introduction

Single-phase face-centered cubic (SP-FCC) alloys normally exhibit good ductility, making them excellent candidates for structural applications, especially at sub-zero temperatures. They are also irreplaceable failure-delaying matrices in a variety of multi-phase or composite engineering materials (e.g., Ni-based superalloys). Designing high-strength SP-FCC alloys bears significant merits toward raising the load-bearing capability of these engineering materials. Conventionally, strengthening of SP alloys relies on introducing various defects that can affect the ability of dislocation initiation or the mobility of dislocations. These defects mainly include dislocations, solutes, and grain boundaries. Among them, a high density of dislocations generated by extensive cold-working may cause dramatic ductility sacrifice. In contrast, solutes and grain boundaries are two crucial mediums that can strengthen SP-FCC materials without a severe sacrifice of the ductility or even in some cases, benefit the

E-mail addresses: Zhao, S. (shijzhao@cityu.edu.hk), Yang, T. (taoyang6-c@my.cityu.edu.hk), Wei, D. (wei1987xiu@imr.tohoku.ac.jp), Gao, Y. (ygao7@utk.edu), Wu, Z. (zwu9@hnu.edu.cn).

 https://doi.org/10.1016/j.mattod.2023.02.012

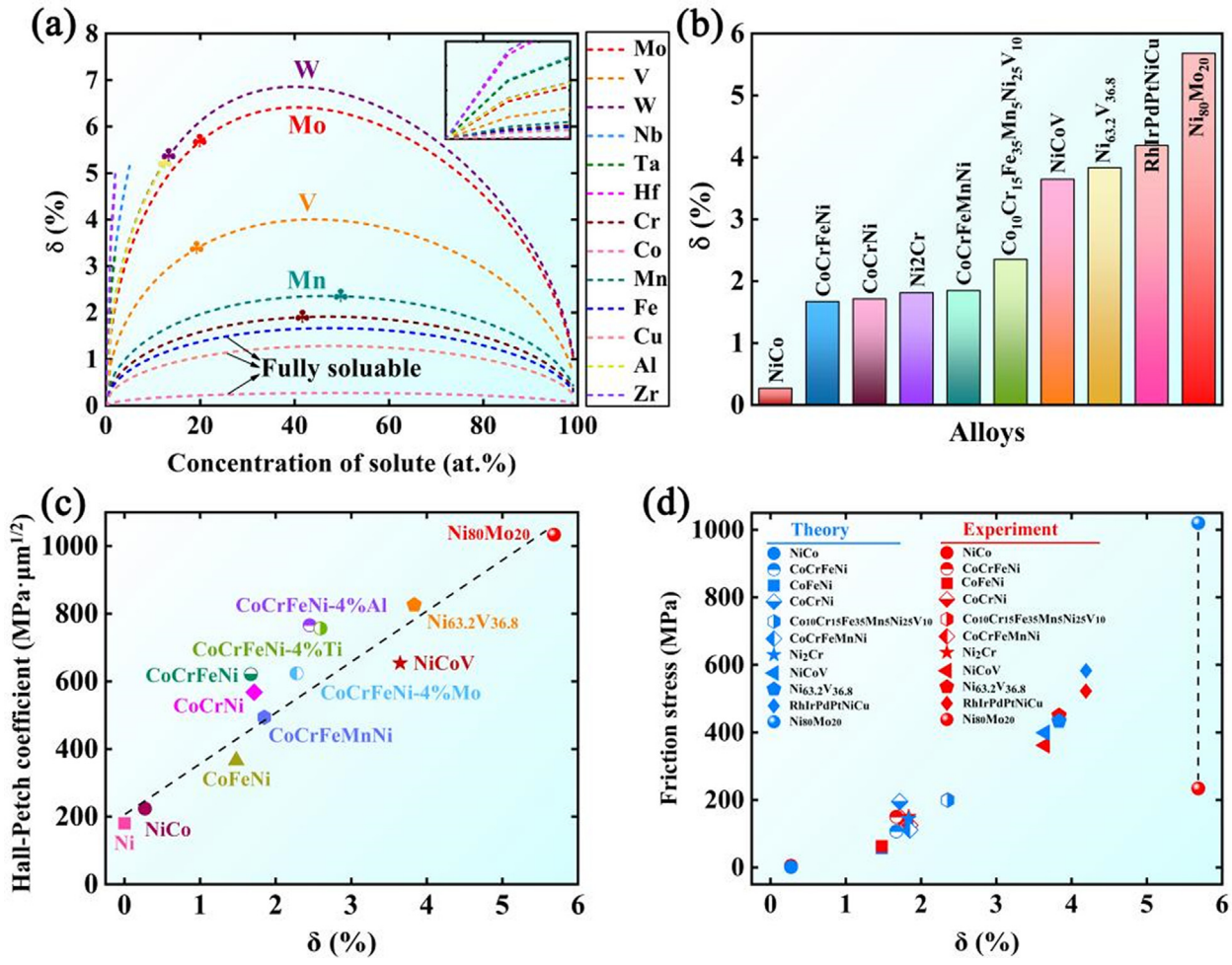

FIGURE 1

(a) the misfit parameter δ of different Ni-based binary alloys as a function of solute concentration. (b) Comparison of the misfit parameter δ of $Ni_{80}Mo_{20}$ with those of other SP-FCC alloys. The correlation of (c) Hall-Petch coefficient and (d) friction stress with δ in SP-FCC alloys.

ductility. Therefore, maximizing these two strengthening contributions is an auspicious approach to design SP-FCC alloys with high strength while maintaining their high ductility.

Solute-induced solid solution strengthening ($\Delta\sigma_{ss}$) arises from the elastic interaction between the stress field of dislocation and the local strain of solute atoms, which affects the dislocation mobility [1–7]. Recent development of high/medium entropy alloys (H/MEAs) [8–19] instigated the design of an increasing number of SP-FCC alloys with high yield strength (σ_y) through taking the greatest advantage of the solute effect by introducing considerable compositional complexity. As representatives, the quinary CoCrFeMnNi alloy [9–14], which is a benchmark HEA, exhibits strength-ductility overall properties outweighing a majority of conventional FCC alloys; one of its sub-alloys, the ternary CoCrNi [10–12,14], which is a statue of MEA, exhibits even better mechanical performance. The strength of CoCrNi was surpassed recently by another MEA, NiCoV, via further boosting the solute effects [12,16] and the property of NiCoV has not been beaten by any other SP-FCC alloys. A multitude of theoretical models [20–30] suggested that $\Delta\sigma_{ss}$ in high/medium entropy as well as conventional SP-FCC alloys is strongly correlated with the volume misfit, which is a structural feature that reflects the average local strain induced by the diverse atomic environments around the constituent element. On the other hand, grain-boundary-induced strengthening ($\Delta\sigma_{gb}$) depends on the extent of stress concentration at boundaries to reach the critical level that can activate the dislocation source in the nearby grains. From the dislocation nucleation mechanism, some recent studies [13,16,31–34] showed that, SP-FCC alloys with more pronounced lattice friction tend to possess higher sensitivity of yield strength to grain size (the so-called Hall-Patch coefficient, k_{HP}). This well indicates the possibility of using volume misfit as a design criterion for high-strength SP-FCC alloys.

Based on the above-mentioned scenarios, here we rely on a misfit-volume-maximization strategy to successfully design a SP-FCC alloy with superb yield strength (~1.05GPa) and good ductility (~37%). The resultant compositionally-simple alloy has a volume misfit severer than all existing SP-FCC alloys, leading to a highest-ever k_{HP} and pronounced $\Delta\sigma_{ss}$. Fundamentally, our work underlines that the misfit volume can be used as a pertinent indicator of k_{HP} and demonstrates that screw dislocations

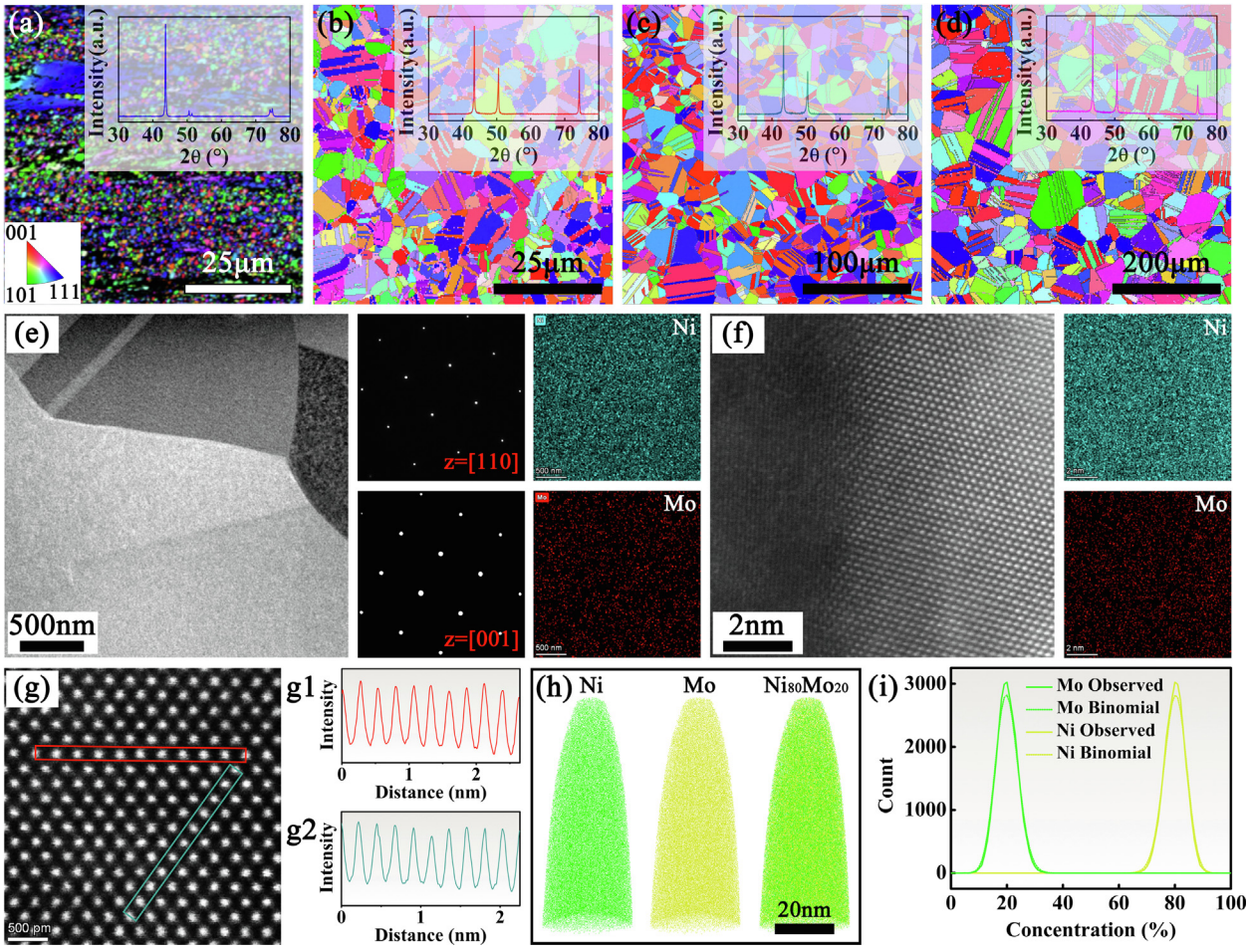

FIGURE 2

Representative microstructure of $Ni_{80}Mo_{20}$. The EBSD inverse pole figure (IPF) maps of $Ni_{80}Mo_{20}$ annealed at (a) 800 °C, (b) 900 °C, (c) 1000 °C, and (d) 1100 °C for 1 h, respectively. The inset shows the corresponding XRD pattern. (e) Low-magnification HAADF-STEM image and (f) High-resolution HAADF-STEM image of $Ni_{80}Mo_{20}$ after annealing at 900 °C for 1 h. The images on the right show the SAED patterns or corresponding STEM-EDS maps. The SAED patterns confirm that the $Ni_{80}Mo_{20}$ is a SP solid solution with a FCC structure. The STEM-EDS maps also verifies that there is no substantial chemical segregation of Ni or Mo or structural transition at the grain boundary. (g) HAADF-STEM micrograph in the grain interiors and (g1, g2) intensity-line profiles of the red and green squared regions in g. (h) 3D APT reconstructions of Ni and Mo atoms. (i) elemental frequency distribution analysis. The absence of local chemical fluctuation was confirmed by the STEM and APT analysis.

can also control the strengthening of SP-FCC alloys with extreme lattice distortion, which is overlooked in previous studies.

Result and discussion

Targeting desirable composition

To search compositions with severe volume misfits, we first consider Ni as the solvent and a variety of transitional metals as solutes, including Hf, Nb, Ta, Mo, W, Cr, Al, Mn, V and Zr. The contribution of the volume misfit to strengthening can be collectively reflected using a δ parameter [5,6,22–27]. Therefore, we quantified δ of the so-formed Ni-based binary alloys through the expression:

$$\delta = \frac{\sqrt{\sum_n c_n \Delta V_n^2}}{3V_{alloy}} \quad (1)$$

where b is the Burgers vector, c_n is the concentration, $\Delta V_n = V_n - V_{alloy}$ is the misfit volume of each type-n constituent element, V_{alloy} is the alloy atomic volume, and V_n is the FCC apparent volume of type-n element in the given alloy. The V_n of each element in the FCC structure were computed using first-principles spin-polarized DFT as implemented in VASP (Table S1) [22,23,26]. The values of V obtained here is 13.9021 $Å^3$, in very good agreement with that reported by Yin et al. [23]. Zr and Hf hold apparent volumes more than twice that of Ni. The FCC apparent volumes of Mo, Al, W, Ta and Nb also are also very large. The so-obtained δ values are presented in Fig. 1a as a function of the concentration of each element. It is found that alloying Co, Fe, Cr and Mn into Ni without exception leads to δ values lower than 2%. In contrast, V is much more efficient in generating larger volume misfits. This may explain why, as Fig. 1b shows, $Ni_{63.2}V_{36.8}$ (δ = 3.834%) and NiCoV (δ = 3.647%) alloy possess much higher $\Delta\sigma_{ss}$ than NiCo (δ = 0.272%), CoCrNi (δ = 1.716%), CoCrFeNi (δ = 1.672%) and CoCrFeMnNi (δ = 1.850%) alloys.

As seen from Fig. 1a, the elements with much larger FCC apparent volumes, including Mo, Al, W, Ta and Nb, can as-expected cause more pronounced volume misfits. It is noteworthy that δ value relies also on the solute concentration. A desirable strengthener should also entail high solubility in Ni.

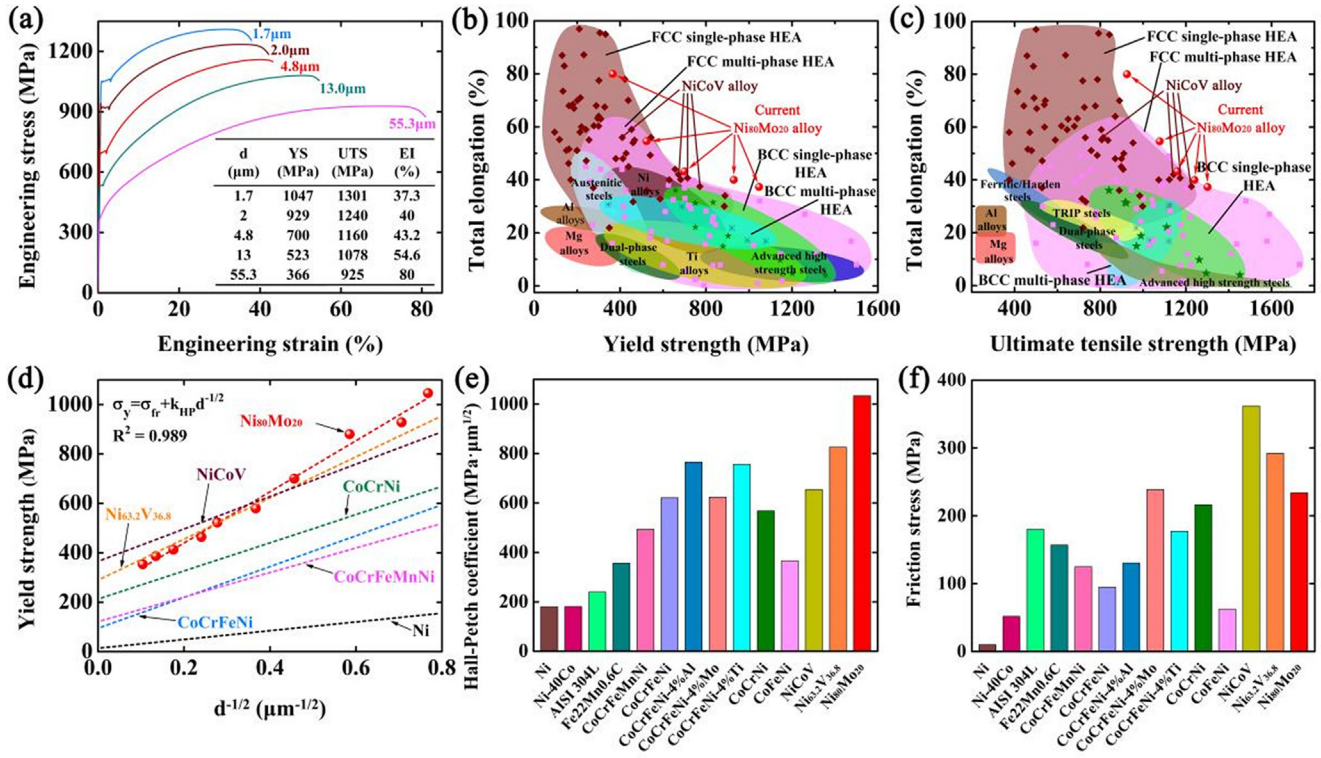

FIGURE 3

Exceptional strength-ductility combination. (a) Representative engineering stress–strain curves of $Ni_{80}Mo_{20}$ with different grain sizes. (b) Yield strength *vs* total elongation and (c) Ultimate tensile strength *vs* total elongation of $Ni_{80}Mo_{20}$ and other metallic materials (Table S2) [37–43]. (d) Dependence of yield strength on the grain size of $Ni_{80}Mo_{20}$ and a few other FCC alloys, including CoCrFeMnNi, CoCrFeNi, CoCrNi, NiCoV, $Ni_{63.2}V_{36.8}$, and Ni (see Figs. S4, S5, and S6 for representative microstructure, engineering stress–strain curves and Hall-Petch relation of NiCoV and $Ni_{63.2}V_{36.8}$, as reproduced in the current study). (e) Hall-Petch coefficient and (f) Friction stress of different SP-FCC materials (Table S3).

Therefore, the solubility of different solute in Ni [35] was extracted and plotted as function of temperature (Fig. S1). The 900 °C-solubility of each solute in Ni was also labeled in Fig. 1a. From this analysis, the $Ni_{80}Mo_{20}$ alloy was eventually targeted as the desired composition. The δ value of this specific alloy reaches 5.68%, higher than any of the existing SP-FCC alloys, including H/MEAs (Fig. 1b). This serves as a good indication that a high-strength SP-FCC alloy may not need considerable compositional complexities.

Forming single phase without significant ordering

The $Ni_{80}Mo_{20}$ alloys were fabricated using arc-melting under an argon atmosphere. 16 mm × 16 mm square ingots of $Ni_{80}Mo_{20}$ were homogenized at 1200 °C for 24 h, followed by cold-rolling to produce ~1.5 mm thick sheets. 800 °C-1 h-annealing results in partial recrystallization (Fig. 2a). A single-phase, fully recrystallized microstructure is achievable by annealing at 900 °C and above (Fig. 2b-d). This unprecedented high recrystallization temperature is in fact the first uniqueness of $Ni_{80}Mo_{20}$. Under the same homogenization and rolling procedures, most other SP-FCC alloys can reach full recrystallization at ~700 °C [13,29,33,36]. The grain sizes of $Ni_{80}Mo_{20}$ annealed at 900 °C, 1000 °C, and 1100 °C for 1 h are 4.8, 13 and 55.3 μm, respectively. A microstructure with an even finer grain (~1.7 μm) can be obtained through 2-minute annealing at 900 °C (Fig. S2).

The SP nature of $Ni_{80}Mo_{20}$ is further confirmed using high-angle annular dark-field scanning transmission electron microscopy (HAADF-STEM) and three-dimensional atom probe tomography (3D APT) taken for the 900 °C-annealed specimen as a representative case (Fig. 2e to i). The Low-magnification HAADF-STEM image of the 900 °C-annealed $Ni_{80}Mo_{20}$ in Fig. 2e and selected-area diffraction (SAED) patterns confirms the absence of any precipitates or long-range ordered (LRO) structure. The corresponding STEM-EDS maps show that Ni and Mo elements are uniformly distributed in the microstructure. High-resolution HAADF-STEM image and corresponding STEM-EDS maps (Fig. 2f) further show that there is no substantial elemental segregation or structural transitions (disordered or ordered) at the grain boundary regions. Fig. 2g displays the HAADF-STEM image in the grain interiors, in which a homogeneous contrast can be seen. From the intensity-line profiles corresponding to the green and red squared regions, no evident deviation (such as an abrupt, significant rise or fall) from the average intensity is observed. Note that such analysis is based on the HAADF Z contrast, and the contrast/intensity is highly sensitive to the atomic mass. Considering the large difference in the atomic masses of Ni and Mo, the observed periodic fluctuation around the average level suggests the absence or insignificance of long-range/short-range ordering (SRO) or other phase (s). Further atomic-resolution EDS maps also show a random distribution of Ni and Mo (Fig. S3). The Ni and Mo atomic maps

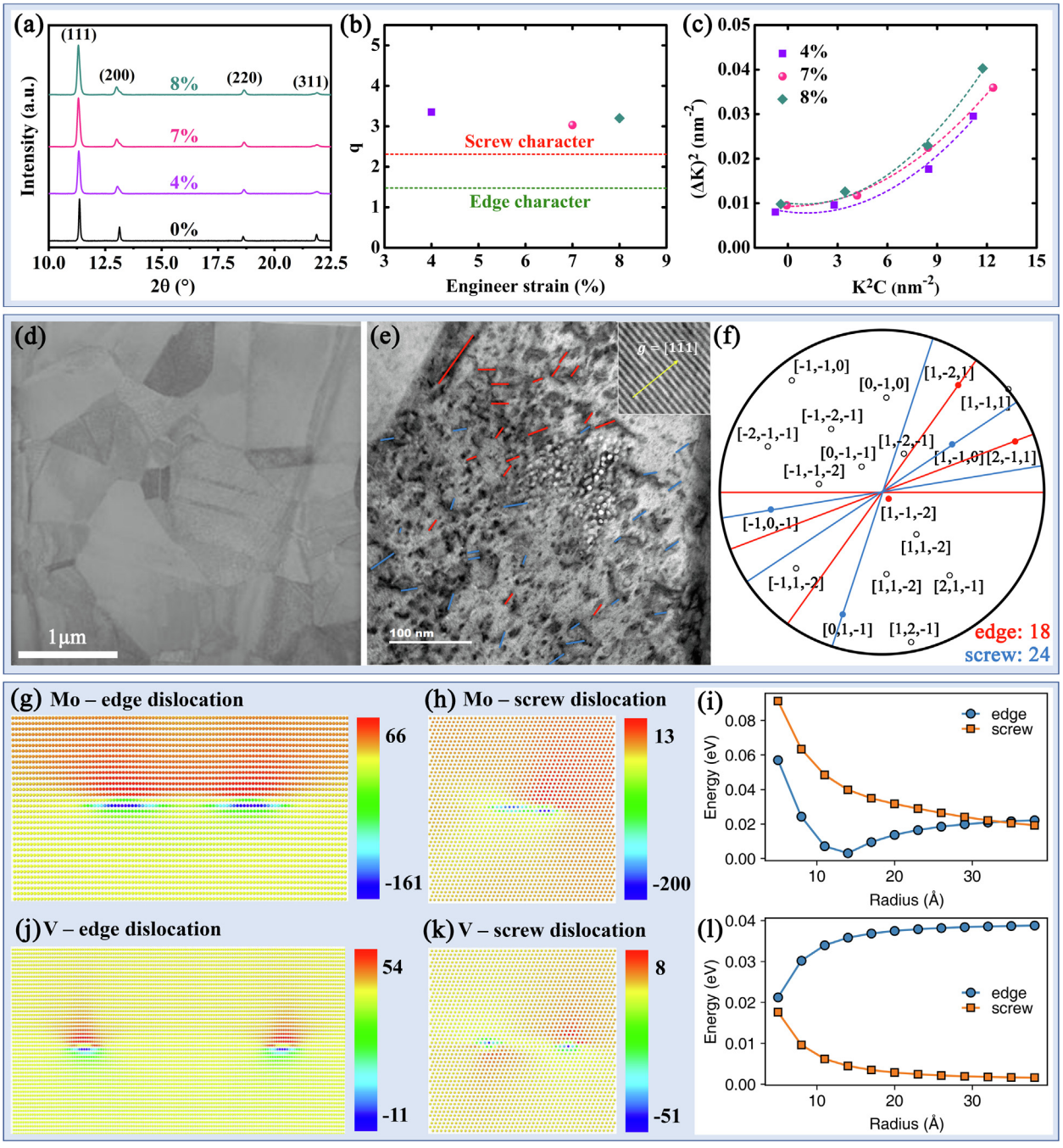

FIGURE 4

Experimental and theoretical justification of active dislocation. (a) High-energy X-ray diffraction patterns of the 900 °C-1 h-annealed $Ni_{80}Mo_{20}$ alloy at an engineering strain of 0%, 4%, 7%, and 8%, respectively. (b) Evolution of dislocation characteristic parameters, q, as a function of engineering strain. The value of q is obtained by Convolutional Multiple Whole Profile (CMWP). (c) Plots of ΔK^2 *vs* K^2C according to the modified Williamson–Hall at engineering strain of 4%, 7%, and 8%, respectively. (d) TEM image and (e) annular-bright-field (ABF)-STEM image of the 900 °C-1 h-annealed $Ni_{80}Mo_{20}$ alloy at a plastic strain of 5% with a two-beam condition near $Z = [1\,\bar{1}\,2]$ and $\vec{g} = [1\,\bar{1}\,1]$. The measured dislocation lines were highlighted. The red and blue lines were edge and screw dislocations, respectively. (f) The corresponding stereographic projection to (e). Interactions between Mo solutes with an edge (g) and screw (h) dislocations in the $Ni_{80}Mo_{20}$ alloy. The values are colored by the interaction energy given by meV. (i) Total interaction energies as a function of the integration radius centered at the dislocation core for Mo in the $Ni_{80}Mo_{20}$ alloy. Interactions between V solutes with edge (j) and screw (k) dislocations in NiCoV. (l) Total interaction energies as a function of the integration radius centered at the dislocation core for V in NiCoV.

from the APT reconstruction are shown in Fig. 2h. The distribution of elements appears to be homogeneous from these maps. Further investigation using the frequency-distribution analysis does not reveal any statistically significant non-random distribution (Fig. 2i). A collective picture drawn from the multi-scale characterization ascertains that $Ni_{80}Mo_{20}$ is a SP solid solution with a FCC structure in which no significant elemental segregation or L/SRO is present.

Exceptional strength-ductility superiority

Fig. 3a shows the representative room-temperature engineering stress–strain curves of $Ni_{80}Mo_{20}$ with different grain sizes. The strength and elongation are summarized in the inserted table. It is seen that, $Ni_{80}Mo_{20}$ with a grain size of ~55.3 μm possesses a σ_y of ~366 MPa, and an ε over 80%. This outperforms most other SP-FCC alloys with similar grain size, such as CoCrNi (σ_y = 282 MPa, ε = 76%) [10]. As the grain size reduces to 2 and 1.7 μm, σ_y of $Ni_{80}Mo_{20}$ skyrockets to ~929 MPa and 1.05 GPA, respectively, while still maintaining an ε of ~37%. We compared the properties of $Ni_{80}Mo_{20}$ with a series of conventional alloys and H/MEAs. From the so-generated "σ_y - ε" (Fig. 3b) and "σ_{UTS} - ε" (Fig. 3c) "banana" diagrams, $Ni_{80}Mo_{20}$ exhibits obvious exceptional strength-ductility superiority that rivals not only SP-FCC alloys, including NiCoV and $Ni_{63.2}V_{36.8}$, but also most other types of alloy, such as multi-phase alloys [37–43].

As a fully-recrystallized, single-phase and SRO-free alloy, the yield stress is a combination of intrinsic lattice resistance to dislocation motion (σ_i), plus two incremental strengthening contributions, $\Delta\sigma_{ss}$ and $\Delta\sigma_{gb}$. σ_i here in $Ni_{80}Mo_{20}$ represents the strength of a pure Ni with an infinite grain size, which was reported to be ~10 MPa [44]. $\Delta\sigma_{ss}$ and $\Delta\sigma_{gb}$ are normally quantified through a classic Hall-Petch treatment of grain-boundary strengthening, in which σ_y is plotted as a function of the inverse square root of grain size ($d^{-1/2}$). Fig. 3d shows such a plot for $Ni_{80}Mo_{20}$. A well linear correlation between σ_y and $d^{-1/2}$ is as expected seen. From the linear fitting (R^2 = 0.989), σ_{fr}, which consists of σ_i and $\Delta\sigma_{ss}$, and the Hall-Petch coefficient (k_{HP}) of $Ni_{80}Mo_{20}$ are derived as ~234 MPa and 1034 MPa·μm$^{1/2}$, respectively.

The Hall-Petch relation as well as k_{HP} and σ_{fr} of a series of single-phase FCC materials, including NiCoV and a few subsets of CoCrFeMnNi, are compared in Fig. 3d-f [13,32–34,44–48]. First, an extreme k_{HP} (1034 MPa·μm$^{1/2}$) is with no doubt the second uniqueness of the investigated $Ni_{80}Mo_{20}$ alloy. This value easily outweighs any of the existing SP-FCC alloys, suggesting the success of current volume-misfit-maximization strategy, at least for the purpose of designing strong SP-FCC alloy relying on grain refinements. A tight positive linear k_{HP} - δ correlation, as observed in Fig. 1c, further indicates the possibility to use the δ parameter as an indicator of k_{HP}. We try to understand this essential role of volume misfit through the dislocation source model of grain boundary strengthening. From the model, the k_{HP} is determined by the critical resolved shear stress (CRSS, τ_c) required for operation of a dislocation source inside a grain as [30,49]

$$k_{HP} = \left(\frac{4G\beta\tau_c}{\beta\pi}\right)^{\frac{1}{2}} \quad (2)$$

where β = 1–ν for edge dislocations (ν = 0.33 is Poisson's ratio) and β = 1 for screws; b = 0.2552 nm and G = 86GPa are the Burgers vector and shear modulus of the investigated $Ni_{80}Mo_{20}$ alloy. It has been shown that CRSS in a SP alloy can be well related to the minimum shear stress required to move a dislocation at 0 K against the lattice friction [16,50,51]. The existence of volume misfit would generate a pressure field around the specific elements [5,6,20,23–26,29]. The pressure field interacts with dislocations to affect their easiness of initiation and/or movement, and the strength of the interaction is linearly dependent on the severity of volume misfit.

Second, σ_{fr} of $Ni_{80}Mo_{20}$ (234 MPa) is also greater than a majority of SP-FCC alloys, such as austenitic steels [47], nickel-base alloy [33], and CoCrFeNi alloy [48], and is comparable to that of CoCrNi [32] and Mo- or Ti-doped CoCrFeNi alloys [48]. Nevertheless, σ_{fr} of $Ni_{80}Mo_{20}$ is ~35% lower than that of NiCoV (362 MPa). This is interesting, since it is expected that a large δ would cause higher $\Delta\sigma_{ss}$ and hence higher σ_{fr}. To show this, based on the calculated δ values and the elastic constants, we predict the σ_{fr} a series of SP-FCC alloys and the currently investigated $Ni_{80}Mo_{20}$. The predicted values of NiCoV, CoCrNi, CoCrFeNi, CoCrFeMnNi, and $Ni_{63.2}V_{36.8}$ alloys match well with those in Yin et al. [23]. As Fig. 1d shows, for most SP-FCC alloys, the predicted values ($\sigma_{fr\text{-}PRED}$) match well with the reported experimental values ($\sigma_{fr\text{-}EXP}$). However for $Ni_{80}Mo_{20}$, $\sigma_{fr\text{-}EXP}$ (234 MPa) has not reached even one-third of its $\sigma_{fr\text{-}PRED}$ (1020 MPa). This significant $\sigma_{fr\text{-}PRED}$-$\sigma_{fr\text{-}EXP}$ deviation accounts for the third uniqueness of $Ni_{80}Mo_{20}$ and is worthy of further elucidation as will be focused in the following sections.

Strength controlled by both types of dislocations

For SP-FCC alloys, the volume-misfit-based solid solution strengthening theories [5,6,21–27] were established by considering the sole contribution of edge dislocations to $\Delta\sigma_{ss}$. The agreement between $\sigma_{fr\text{-}EXP}$ and $\sigma_{fr\text{-}PRED}$ for most FCC alloys, such as NiCoV and CoCrNi, thus signifies the dominant role of edge dislocations in them. For $Ni_{80}Mo_{20}$, the dramatic $\sigma_{fr\text{-}EXP}$ - $\sigma_{fr\text{-}PRED}$ deviation indicates the breakdown of the assumption. In other words, screw dislocations may also serve to strengthen $Ni_{80}Mo_{20}$. To further understand this trend, we trace back to the classical Labusch model [2,3,12,29,48], which integrated contributions from both types of dislocations. By considering the atomic-size misfit ($\varepsilon_a = \frac{1}{a}\frac{da}{dc}$, a is the lattice constant) and modulus (G) mismatch ($\varepsilon_G = \frac{1}{G}\frac{dG}{dc}$) between the solute and solvent atoms, the model has an expression:

$$\Delta\sigma_{SS} = fG_{solv}\varepsilon^{\frac{4}{3}}c^{\frac{2}{3}} \quad (3)$$

where f is a dimensionless fitting parameter, G_{solv} is the shear modulus of the solvent, $\varepsilon = \left[\left(\frac{\varepsilon_G}{1+0.5|\varepsilon_G|}\right)^2 + \alpha^2\varepsilon_a^2\right]^{\frac{2}{3}}$ represents the overall contributions from the elastic misfit, α is a dimensionless parameter that describes the type of dislocations, α = 3 for screw dislocations, and α = 16 for edge dislocations [3,12,48].

Recognizing the dominating role of edge dislocations (α = 16) in Ni-50%Co and Ni-33.3%Cr binary alloys [23], with their known $\Delta\sigma_{ss}$, a, and G, and by assuming linear c-a and c-G relations, we quantified f for Ni-50%Co (0.0081) and Ni-33.3%Cr (0.0058) and applied the average value (f = 0.00695) to $Ni_{80}Mo_{20}$. ε_a and ε_G *in* $Ni_{80}Mo_{20}$ were determined from a and G of Ni [10] (3.5267 Å, 76GPa) and $Ni_{80}Mo_{20}$ (3.6089 Å, 86GPa). By feeding f, G, ε_a, and ε_G, the Labusch model predicts a $\Delta\sigma_{ss}$ of ~85 MPa and 353 MPa for $Ni_{80}Mo_{20}$, using an α value of 3 and 16, respectively. From the differences in σ_{fr} between the pure Ni and $Ni_{80}Mo_{20}$, $\Delta\sigma_{ss}$ in $Ni_{80}Mo_{20}$ is determined to be ~224 MPa. The falling of this experimentally obtained $\Delta\sigma_{ss}$ within the predicted range (85–353 MPa) suggests the active role of both types of dislocations.

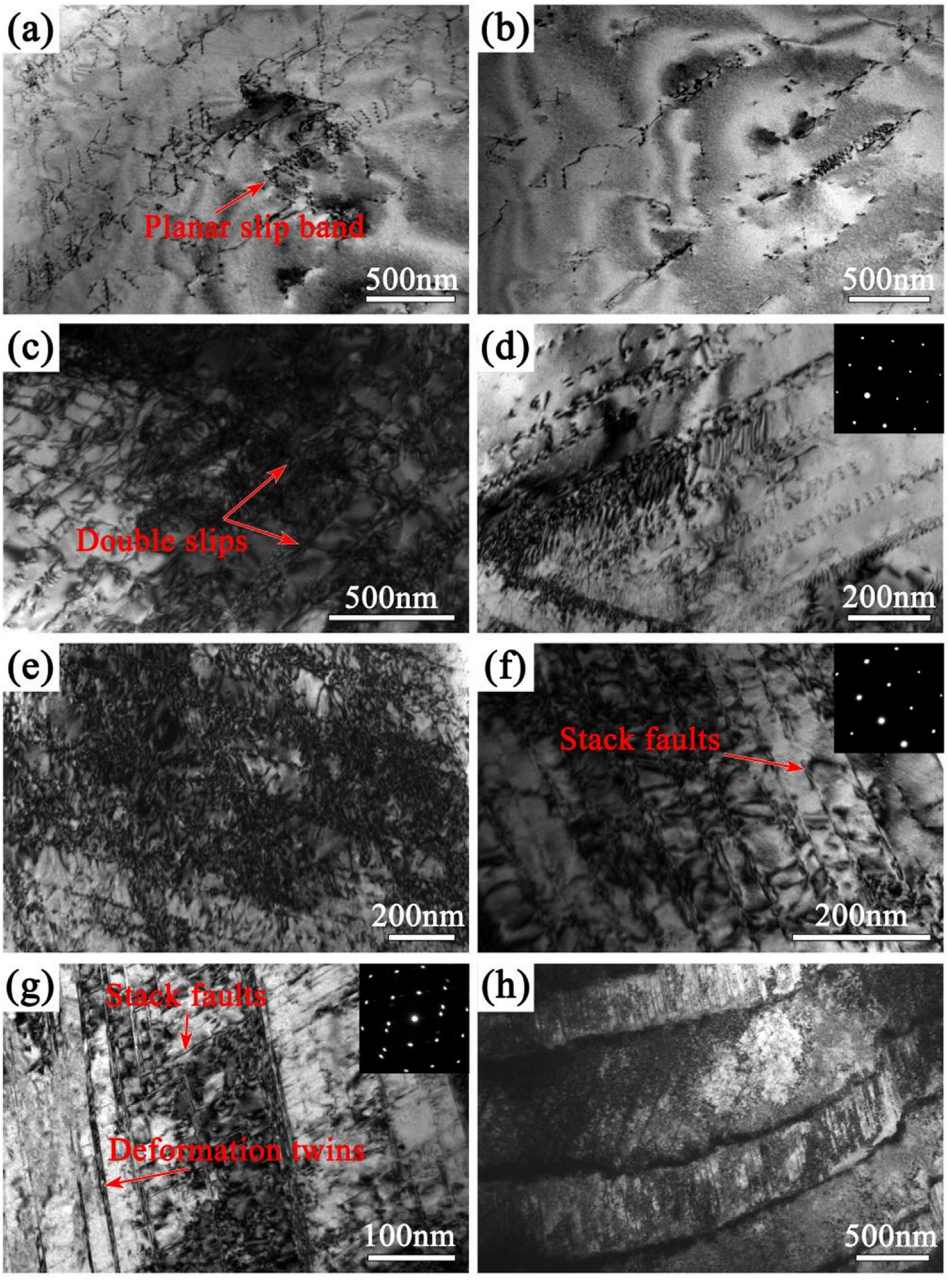

FIGURE 5

Deformation microstructures of the $Ni_{80}Mo_{20}$ alloy with a grain size of 4.8 μm at tensile strains of (a,b) 2%, (c,d) 15%, (e,f) 22.5%, and (g,h) fracture. The SAED pattern taken from [110] zone axis.

Experimental and theoretical justification of active dislocation

We follow the method of the XRD line broadening to reveal the dislocation characteristic parameters, q [52,53]. To achieve this, we captured the XRD patterns (Fig. 4a) of $Ni_{80}Mo_{20}$ (900 °C-1 h-annealed) with different engineering strains (0%, 4%, 7%, and 8%) using in-situ synchrotron high-energy X-ray diffraction (HEXRD) and compared the q values obtained using Convolutional Multiple Whole Profile (CMWP) [54,55] procedures with the theoretical value for edge dislocations (q = 1.5) and screw dislocations (q = 2.3), which were determined based on the elastic constants (C_{11}, C_{12}, and C_{44}) of $Ni_{80}Mo_{20}$. As shown in Fig. 4b, the q values (3.031–3.352) revealed experimentally match better with that for screw dislocations, suggesting the non-ignorable role of screw dislocations in the strengthening and deformation of $Ni_{80}Mo_{20}$. Further analysis via the modified Williamson - Hall analysis [53,56] (Fig. 4c) yields a consistent conclusion.

Moreover, we try to provide a direct observation of the types of mobile dislocations in $Ni_{80}Mo_{20}$. To this end, a $Ni_{80}Mo_{20}$ specimen (900 °C-1 h-annealed) tensile-deformed to 5% engineering strain was characterized via bright-field scanning transmission microscopy (BF-STEM) and stereographic analysis, following the method in research by Lee et al. [52] and Feng et al. [21]. Note

that the Burgers vector of perfect dislocations in the FCC structure is 1/2[110]. That is, the corresponding dislocation line vectors of edge and screw types are 1/2[112] and [110], respectively. The dislocation line would be chosen if it satisfies the length (>5nm) and degree difference (<5 degrees). The direction of chosen lines was compared to stereographic projection, and the dislocation type was determined. The results are shown in Fig. 4d-f. The number of screw dislocations occupied more of all measured dislocation lines (24 of 42, or 57%), suggesting the active or even predominant role of the screw character in $Ni_{80}Mo_{20}$.

To theoretically understand the role of different dislocations, the solute-dislocation interactions are calculated through molecular statistics. $Ni_{80}Mo_{20}$ and NiCoV were investigated for comparison purposes. Here we consider both edge and screw dislocations with b = [110]/2. The obtained interaction energy, $U_n(x_i, y_i)$, for each element in the two alloys is provided (Fig. S7 and S8). Fig. 4g-l present the interaction energy of Mo and V with edge and screw dislocations. It is clear that, the interaction energy of Mo (-161 and −200 meV in the core for edge and screw dislocations, respectively) in $Ni_{80}Mo_{20}$ is much larger than V (-11 and −51 meV in the core for edge and screw dislocations, respectively) in NiCoV, consistent with the large misfit volume of Mo, according to $U_n(x_i, y_i) = -p(x_i, y_i)\Delta V_n$, where $p(x_i, y_i)$ is the pressure field around the dislocation.

To gain further insight into the overall interaction contributions of solutes with different dislocations, we have integrated the obtained interaction energies around the dislocation core (centered at one of the two partials) for both edge and screw dislocations. The results for Mo in $Ni_{80}Mo_{20}$ (Fig. 4i) and V in NiCoV (Fig. 4l) are compared, as these two elements dominate the interactions. The results demonstrate that in NiCoV the solute-screw dislocation interactions are much weaker than the solute-edge dislocation interactions, suggesting the dominating role of the edge dislocation in terms of strengthening. In contrast, in $Ni_{80}Mo_{20}$, the total interaction energy with screw dislocations is even higher than those with edge dislocations, signifying the vital role of the screw dislocation in the alloy.

Differences in the contribution from screw dislocations can be rationalized through the effects of solutes on the spherical symmetry of the stress fields generated by solutes. In dilute alloys, each solute atom is surrounded by identical solvent atoms. Thus, the stress field created by the solute atom is spherically symmetric and contains no shear stress component. They therefore do not interact with screw dislocations due to their pure shear nature. In concentrated alloys, the atoms surrounding a certain type of solute will no longer be the same. In this case, if each constituent element has a similar atomic size, the spherical symmetry can still be retained. This trend explains why edge dislocations dominate in the CoCrFeMnNi alloy and its suballoys, such as NiCo and CoCrNi. In contrast, if the constituent atoms differ largely in the atomic size, the spherical symmetry will be reduced. This is the case for both NiCoV and $Ni_{80}Mo_{20}$, in which there is a type of element whose atomic size (V and Mo) is obviously larger than the others. Compared to V, Mo has more pronounced differences than V in atomic sizes with other constituent elements (Co and/or Ni). As a consequence, the stress field in $Ni_{80}Mo_{20}$ would be less spherical than that in NiCoV. A collective analysis of $Ni_{80}Mo_{20}$ and NiCoV indicates the presence of a critical nonsphericity beyond which screw dislocations would play a noticeable role in strengthening. A further theoretical framework is needed to quantify this threshold.

Multiple consecutive strain-hardening mechanisms

We performed TEM characterizations on the 900 °C-1 h-anneal ed $Ni_{80}Mo_{20}$ alloy, as a representative, at different deformation stages to understand the origin of high ductility. At the initial stage (~2%) of plastic deformation (Fig. 5a-b), the dislocation-slip mode is dominated by planar slip, as evidenced by the formation of numerous planar-slip bands. At ~15% deformation, dense dislocation networks and multiple non-coplanar slip systems are activated (Fig. 5c-d). Upon further deforming to ~22.5%, extensive SFs emerge and dominate, some deformation twins (DTs) are also observed, as confirmed by the SAED pattern in Fig. 5e-f and Fig. S9. Fig. 5g-h reveal the deformed microstructure at the tensile failure. At this stage, a tremendous amount of DTs formed (Fig. 5g and Fig. S9). All of the observed features, including the planar-slip dislocation configuration at the preliminary stage, SFs at the intermediate stage, and DTs at the late stage, are beneficial for the alloy's strain-hardening capability [10–12,29,57–59] and are signatures of the alloy's medium-to-low SFE, as supported by our DFT calculations, which shows that the SFEs of $Ni_{80}Mo_{20}$ is ~45 mJ/m^2. An important phenomenon that is worthy of special mention is that, upon failure, a special dislocation structure, parallel-distributed extended dislocation walls, can be seen (Fig. 5h). These features can benefit the strain-hardening capability and tensile ductility in twofold manners. First, the walls have a large dislocation-storage capacity, as suggested by its containment of high-density dislocations (Fig. 5h), which is critical for increasing the work-hardening capability according to the classic plastic-deformation theory. Next, the walls uniformly subdivide the grains and, on the one hand, consequently, disperse the local strain concentration and homogenize the plastic deformation. The active role of SFs and DTs is also observed in the deformation of finer-grained and coarser-grained $Ni_{80}Mo_{20}$ alloys (Fig. S10 and S11).

Conclusion

In the present work, a compositionally-simple single-phase FCC alloy with a superb strength (~1.05GPa) and a good ductility (37%) is designed through maximizing the volume misfits. The targeted $Ni_{80}Mo_{20}$ alloy has a volume misfit (δ = 5.68%) severer than any existing FCC alloy, including both conventional alloy and high/medium entropy alloys. The unprecedented volume misfits lead to a highest-ever sensitivity of strength to grain size (k_{HP} = 1034 MPa·μm$^{1/2}$), making this alloy extremely strengthenable through grain refinements. The severe volume misfit also brings the alloy a high solid solution strengthening, though current δ-based strengthening theories fail to reproduce the experiment values due to the proven active role of screw dislocations in controlling the strengthening, as demonstrated by means of a variety of theoretical and experimental techniques. Overall, the current findings pave a novel avenue for designing more advanced out-performing FCC alloys by maximizing and well

balancing contributions from solutes and grain boundaries through the volume-misfit-maximization strategy.

Materials and methods

Alloy fabrication

The $Ni_{80}Mo_{20}$ alloy was produced by arc melting and drop-casting. The cast ingots underwent a series of thermomechanical processing, including homogenization (1200 °C, 24 h, water quenching), cold-rolling (~90% thickness reduction), and further heat treatments (800 – 1100 °C, water quenching).

Physical characterization

The phase component was characterized, using X-ray diffraction (XRD) in a Panalytical XPert PRO MRD goniometer equipped with Cu-Kα radiation (20 – 100°, 5°/min., step size: 0.01°). The microstructure was characterized by a field-emission scanning electron microscope (FE-SEM, TESCAN MIRA3 LMH) with electron backscatter diffraction (EBSD) and transmission electron microscope (TEM, JEOL 2100F). For SEM observations, the specimens were ground through 2000-grit SiC papers, followed by a two-step vibromet polishing (Buehler Vibromet 2), using aluminum-oxide suspensions and colloidal silica suspension, respectively. For TEM analyses, the specimens were first ground to ~50 μm and then punched to Φ-3 mm discs, followed by jet-polishing and Ar-ion cleaning. Atomic-resolution high-angle annular dark-field (HAADF)-scanning transmission electron microscopy (STEM, Themis Z 3.2) and atom probe tomography (APT, CAMECA LEAP 5000 XR) were performed to analyze the chemical homogeneity on an atomic scale, where the specimen was prepared, using a dual-beam focused ion beam (FIB/SEM, Helios 5 CX). An Image Visualization and Analysis Software package (IVAS 3.8) was used for three-dimensional reconstructions and data analysis. Microstructures of tensile specimens after deformation were also characterized using TEM. Tensile tests were conducted at an engineering strain rate of $1 \times 10^{-3} s^{-1}$, using a SHIMADZU AGS-X 50KN tensile testing machine at room temperature. A full-range extensometer (SHIMADZU Non-Contact Digital Video Extensometer) was utilized for strain measurements.

Shear modulus was measured using resonant ultrasound spectroscopy (RUS) at room temperature [10]. The bright-field STEM images were acquired on JEOL ARM200F TEM/STEM with spherical-aberration correctors. The dislocation types in the images were identified by stereographic analysis [52]. In-situ high-energy X-ray diffraction experiments were performed at the beamline, BL46XU, of SPring-8 in Japan. The wavelength of the X-ray beam was 0.4131 Å (energy: 30 keV), and the beam size was 500 μm × 300 μm. The strain rate of the uniaxial tensile was $\sim 1 \times 10^{-3}$ s^{-1}. More details of the experiments can be seen elsewhere [60]. The convolutional multiple whole profile (CMWP) method was used to analyze the dislocation characteristic parameters q [52].

Theoretical calculations

The density functional theory (DFT) calculations were performed using the VASP package [61,62]. The exchange and correlation interactions were described by the generalized gradient approximation (GGA) in the Perdew, Burke, and Ernzerhof (PBE) form [63]. In this study, we mainly consider the ferromagnetic (FM) states of the interested alloys. Therefore, spin polarization was considered for all calculations. The energy cutoff was set to 400 eV. For structural relaxation, the convergence criteria were 10^{-4}eV for the energy and 0.01 eV/Å for atomic forces, respectively. To model the random solid solutions considered in the present work, special quasirandom structures (SQSs) were built with a Monte-Carlo algorithm by optimizing the short-range order (SRO) parameters close to zero [64,65].

Stacking-fault (SF)-energies calculations were carried out employing the supercell method, as detailed in our previous study [64]. Specifically, a SQS oriented along the [112], $[\bar{1}\,10]$, and $[\bar{1}\,\bar{1}\,1]$ directions were constructed first. Then, a vacuum layer larger than 10 Å is added to it, and an SF is introduced by rigidly shifting the upper $[\bar{1}\,\bar{1}\,1]$ layers with respect to the lower half along the Burgers vector direction. After the shift, the atomic positions were relaxed along the close-packed direction only. The SFE was calculated by:

$$SFE = \frac{1}{A}(E_{SF} - E_0) \quad (4)$$

where E_{SF} and E_0 are the energies for the configurations with and without SF, respectively, and the SF area is A. It is known that the SFE calculated from the supercell method depends on the local atomic arrangement near the SF [66]. To obtain the distribution of SFEs, a total of 3 SQS supercells were used for calculations, generating a total of 27 SFE values for each alloy.

Apparent volumes of elements in FCC alloys were calculated by optimizing the volume and atomic positions simultaneously until the force on each atom was lower than 0.01 eV/Å. The final obtained structures were used to deduce the apparent atomic volumes for each element. The calculation results are listed in Table S1.

Solute-dislocation interactions were calculated through molecular statistics using the Large-scale Atomic/Molecular Massively Parallel Simulator (LAMMPS) [67]. The embedded atom method (EAM) potential proposed by Zhou et al. [68] was used to describe the interactions in $Ni_{80}Mo_{20}$ and NiCoV. This set of potentials has been extensively utilized to model HEAs previously [69]. To compute the interaction energy in random solid solutions, we constructed an average atom potential for the considered $Ni_{80}Mo_{20}$ and NiCoV alloys [70]. The average atom potential bears the average properties of the true random alloy. Within this averaged medium, an individual alloying atom was used to substitute into different lattice positions around dislocations, and the energy difference before and after substitution was recorded. This energy difference can then be used to calculate the solute-dislocation interactions at different locations [5]. Here we considered both edge and screw dislocations with b = [110]/2. For edge dislocation, the supercell size used in the simulation was around 385 × 374 × 44 $Å^3$ along the X[110], Y$[\bar{1}\,11]$, and Z$[1\,\bar{1}\,2]$ directions, respectively. Periodic-boundary conditions were applied along the X and Z directions. The size was around 267 × 251 × 51 $Å^3$ along the X$[1\,\bar{1}\,2]$, Y$[\bar{1}\,11]$, and Z[110] directions, respectively. Periodic-boundary conditions were applied along the X and Z directions, with a tilt factor, as suggested in

previous studies [71]. The dislocation line was along the Z direction in both cases.

Estimation of friction stress

We adopted the solid-solution strengthening theory from Yin et al. [23] to evaluate the friction stress of the considered alloys. In this model, the alloying elements are regarded as solutes that interact with a dislocation in an averaged matrix that can represent the averaged macroscopic properties of the disordered alloy. By virtue of the elasticity theory and ignoring the details of the dislocation core, the solute-dislocation interaction energy can be directly calculated by $-p(x, y)\Delta V_n$, where $p(x, y)$ is the elastic pressure field at the position (x, y), and ΔV_n is the average misfit volume for the type n element. In FCC and BCC alloys, the model results provide the zero-temperature shear yield stress τ_{y0} and the activation energy barrier ΔE_b, as:

$$\tau_{y0} = A_\tau \alpha^{-\frac{1}{3}} \mu \left[\frac{1+\nu}{1-\nu}\right]^{\frac{4}{3}} \left[\frac{\sum_n c_n \Delta V_n^2}{b^6}\right]^{\frac{2}{3}} \tag{5}$$

$$\Delta E_b = A_E \alpha^{\frac{1}{3}} \mu b^3 \left[\frac{1+\nu}{1-\nu}\right]^{\frac{2}{3}} \left[\frac{\sum_n c_n \Delta V_n^2}{b^6}\right]^{\frac{1}{3}} \tag{6}$$

The standard thermal activation theory then leads to the predicted tensile yield stress as follows, at temperature, T, and strain rate, $\dot{\varepsilon}$.

$$\sigma_y(T, \dot{\varepsilon}) = 3.06\tau_{y0}\left[1 - \left(\frac{kT}{\Delta E_b} \ln\left(\frac{\dot{\varepsilon}_0}{\dot{\varepsilon}}\right)\right)^{\frac{2}{3}}\right] \tag{7}$$

where the 3.06 is the Taylor factor. $\dot{\varepsilon}_0 = 10^4 s^{-1}$, b is the Burgers vector, and the values was taken as $b = \frac{\sqrt{2}}{2}a$ based on the FCC lattice parameters. μ and ν are the shear modulus and Poisson's ratio. α = 0.125 (FCC) or 0.0833(BCC) is the line-tension paramater for the edge dislocation. Calculations [22] of the typical atomistic structures of the edge dislocation give the prefactor coefficients (A_τ, A_E) = (0.01785, 1.5618) for FCC alloys and (A_τ, A_E) = (0.040, 2.00) for BCC alloys. The misfit volumes ΔV_n of the constituent element, n, in alloy at composition $\{c_n\}$ can be calculated,

$$\Delta V_n = V_n - V_{alloy} \tag{8}$$

Where V_n is the apparent volume of the constituent element, n, in the given crystal structure. The alloy atomic volume V_{alloy} is estimated by applying Vegard's law, i.e., $V_{alloy}=\sum_n c_n \Delta V_n^2$. Then the misfit parameter δ is estimated,

$$\delta = \frac{\sqrt{\sum_n c_n \Delta V_n^2}}{3V_{alloy}} \tag{9}$$

Determination of dislocation types

We have performed the broadening analysis of diffraction peak by using the in situ synchrotron HEXRD technique to demonstrate that screw dislocations can control the plastic flows during tensile deformation in $Ni_{80}Mo_{20}$ alloy. Recently, the XRD line broadening has been conducted and applied to FCC and BCC alloys such as 304 steel [72], NbTaTiV and CrMoNbV HEAs [52] to reveal the dislocation character. Noted that line broadening of diffraction peak during deformation contributed from size broadening and strain broadening [53,73]. The degree of strain broadening is related to dislocation type and dislocation density. The full-width at half-maximum (FWHM) of line profiles obtained from diffraction peak is substituted into the following modified Williamson–Hall equation [73]:

$$\Delta K \cong \frac{0.9}{D} + \left(\frac{\pi M^2 b^2}{2}\right)^{\frac{1}{2}} \rho^{\frac{1}{2}} K C^{\frac{1}{2}} + O\left(KC^{\frac{1}{2}}\right)^2 \tag{10}$$

Where ΔK is the FWHM and M is a constant. D, b, and ρ represent the average grain size, the Burgers vectors of dislocations, and the dislocation density, respectively. $K = 2\sin\theta/\lambda$ (here, θ, λ is the diffraction angle and the wavelength of X-rays, respectively). O stands for higher order terms in $KC^{1/2}$. In a polycrystalline cubic crystals, the average contrast factors C are calc

$$C = C_{h00}(1 - qH^2) \tag{11}$$

Where C_{h00} is a constant depending on the elastic constants C_{11}, C_{12} and C_{44} of the materials. For a given {hkl} plane, $H^2 = (h^2k^2 + k^2l^2 + h^2l^2)/(h^2 + k^2 + l^2)^2$. Here, q is a character parameter of the dislocation depending on the relative fractions of screw and edge dislocations.

The cubic elastic constants, C_{11}, C_{12}, and C_{44} for $Ni_{80}Mo_{20}$, are carried out by DFT calculations, and the results are 258 GPa, 180 GPa, and 109 GPa, respectively. The resulting elastic anisotropy $2C_{44}/(C_{11} - C_{12})$ = 2.79487 and the ratio C_{11}/C_{44} = 1.65138. Therefore, the theoretical value of q is 1.5 for edge dislocations, and the theoretical value of q is 2.3 for screw dislocations in $Ni_{80}Mo_{20}$. Having analyzed the nature of the peak broadening, the Convolutional Multiple Whole Profile (CMWP) method was applied to reveal the q value at different strain levels [52–54].

Author contributions

Z.W conceptualized and initiated the project. Z.L prepared samples and carried out microstructural characterizations as well as mechanical tests. S.Z and S.M performed calculations and data analysis. T.Y supervised and Q.L conducted APT experiments, post-deformation microstructural characterization and data analysis. Y.-C.C, P.K.L, C.-Y.W carried out the Bright-Field (BF)-Scanning Transmission Electron Microscopy (STEM) and Stereographic analysis. D.W conducted in-situ synchrotron high-energy X-ray diffraction (HEXRD) tests. D.W and Z.L analyzed the HEXRD data. Z.L wrote the draft and all authors contributed to the discussion and revision of the manuscript.

Data availability

Data will be made available on request.

Declaration of Competing Interest

The authors declare that they have no known competing financial interests or personal relationships that could have appeared to influence the work reported in this paper.

Acknowledgments

The present work was supported financially by the National Key R&D Program of China (No. 2022YFE0200900). SZ acknowledges the support from Research Grants Council of Hong Kong (No. 11200421). TY greatly acknowledges the financial supports from the National Natural Science Foundation of China (No. 52101151). We also appreciate Dr. J.H. Luan for the support on the 3D-APT test. PKL very much appreciates the supports from (1) the National Science Foundation (DMR-1611180 and

1809640) and (2) the US Army Research Office (W911NF-13–1-0438 and W911NF-19–2-0049).

Appendix A. Supplementary material

Supplementary data to this article can be found online at https://doi.org/10.1016/j.mattod.2023.02.012.

References

[1] R.L. Fleischer, Acta Metall. 11 (1963) 203–209, https://doi.org/10.1016/0001-6160(63)90213-X.
[2] R.A. Labusch, Phys. Status Solidi. 41 (1970) 659–669, https://doi.org/10.1002/pssb.19700410221.
[3] Z. Wu, Y. Gao, H. Bei, Acta Mater. 120 (2016) 108–119, https://doi.org/10.1016/j.actamat.2016.08.047.
[4] E. Clouet, Acta Mater. 54 (2006) 3543–3552, https://doi.org/10.1016/j.actamat.2006.03.043.
[5] C. Varvenne et al., Acta Mater. 124 (2017) 660–683, https://doi.org/10.1016/j.actamat.2016.09.046.
[6] G. Bracq et al., Acta Mater. 177 (2019) 266–279, https://doi.org/10.1016/j.actamat.2019.06.050.
[7] S. Nag, W.A. Curtin, Acta Mater. 200 (2020) 659–673, https://doi.org/10.1016/j.actamat.2020.08.011.
[8] J.W. Yeh et al., Adv. Eng. Mater. 6 (2004) 299–303, https://doi.org/10.1002/adem.200300567.
[9] B. Gludovatz et al., Science 345 (2014) 1153–1158, https://doi.org/10.1126/science.1254581.
[10] Z. Wu et al., Acta Mater. 81 (2014) 428–441, https://doi.org/10.1016/j.actamat.2014.08.026.
[11] E.P. George, D. Raabe, R.O. Ritchie, Nat. Rev. Mater. 4 (2019) 515–534, https://doi.org/10.1038/s41578-019-0121-4.
[12] W. Li et al., Prog. Mater. Sci. 118 (2021), https://doi.org/10.1016/j.pmatsci.2021.100777 100777.
[13] F. Otto et al., Acta Mater. 61 (2013) 5743–5755, https://doi.org/10.1016/j.actamat.2013.06.018.
[14] B. Gludovatz et al., Nat. Commun. 7 (2016) 10602, https://doi.org/10.1038/ncomms10602.
[15] P. Shi et al., Mater. Today 41 (2020) 62–71, https://doi.org/10.1016/j.mattod.2020.09.029.
[16] S.S. Sohn et al., Adv. Mater. 31 (2019) 1807142, https://doi.org/10.1002/adma.201807142.
[17] X. Chen et al., Nature 592 (2021) 712–716, https://doi.org/10.1038/s41586-021-03428-z.
[18] C. Lee et al., Adv. Mater. 32 (2020) 2004029, https://doi.org/10.1002/adma.202004029.
[19] R.K. Nutor et al., Sci. Adv. 7 (2021) eabi4404, https://doi.org/10.1126/sciadv.abi4404.
[20] G.P.M. Leyson et al., Nature Mater. 9 (2010) 750–755, https://doi.org/10.1038/nmat2813.
[21] R. Feng et al., Adv. Mater. 33 (2021) 2102401, https://doi.org/10.1002/adma.202102401.
[22] C. Varvenne, A. Luque, W.A. Curtin, Acta Mater. 118 (2016) 164–176, https://doi.org/10.1016/j.actamat.2016.07.040.
[23] B. Yin, F. Maresca, W.A. Curtin, Acta Mater. 188 (2020) 486–491, https://doi.org/10.1016/j.actamat.2020.01.062.
[24] B. Yin, W.A. Curtin, Mater. 5 (2019) 1–7, https://doi.org/10.1038/s41524-019-0151-x.
[25] B. Yin et al., Nat. Commun. 11 (2020) 2507, https://doi.org/10.1038/s41467-020-16083-1.
[26] B. Yin, W.A. Curtin, Mater. Res. Lett. 8 (2020) 209–215, https://doi.org/10.1080/21663831.2020.1739156.
[27] W.G. Nöhring, W.A. Curtin, Scr. Mater. 168 (2019) 119–123, https://doi.org/10.1016/j.scriptamat.2019.04.012.
[28] H.S. Oh et al., Nat. Commun. 10 (2019) 2090, https://doi.org/10.1038/s41467-019-10012-7.
[29] E.P. George, W.A. Curtin, C.C. Tasan, Acta Mater. 188 (2020) 435–474, https://doi.org/10.1016/j.actamat.2019.12.015.
[30] C. Wagner, G. Laplanche, Acta Mater. 244 (2023), https://doi.org/10.1016/j.actamat.2022.118541 118541.
[31] R. Armstrong et al., Philos. Mag. 7 (1962) 45–58, https://doi.org/10.1080/14786436208201857.
[32] Y.L. Zhao et al., Acta Mater. 138 (2017) 72–82, https://doi.org/10.1016/j.actamat.2017.07.029.
[33] S. Yoshida et al., Scr. Mater. 134 (2017) 33–36, https://doi.org/10.1016/j.scriptamat.2017.02.042.
[34] F. de las Cuevas et al., Key Eng. Mater. 423 (2010) 147–152, https://doi.org/10.4028/www.scientific.net/KEM.423.147.
[35] , ASM International, Ohio, 1990.
[36] Z. Wu et al., Intermetallics 46 (2014) 131–140, https://doi.org/10.1016/j.intermet.2013.10.024.
[37] T.J. Jang et al., Nat. Commun. 12 (2021) 4703, https://doi.org/10.1038/s41467-021-25031-6.
[38] D. Wei et al., Acta Mater. 225 (2022) 117571, https://doi.org/10.1016/j.actamat.2021.117571.
[39] J. Li et al., J. Mater. Sci. Technol 131 (2022) 185–194, https://doi.org/10.1016/j.jmst.2022.06.003.
[40] J. Rackwitz et al., Acta Mater. 200 (2020) 351–365, https://doi.org/10.1016/j.actamat.2020.09.021.
[41] D.G. Shaysultanov et al., J. Alloys Compd. 705 (2017) 756–763, https://doi.org/10.1016/j.jallcom.2017.02.211.
[42] H. Huang et al., Adv. Mater. 29 (2017) 1701678, https://doi.org/10.1002/adma.201701678.
[43] Y. Wu et al., Mater. Sci. Eng. A 724 (2018) 249–259, https://doi.org/10.1016/j.msea.2018.03.071.
[44] Y.Y. Zhao, T.G. Nieh, Intermetallics 86 (2017) 45–50, https://doi.org/10.1016/j.intermet.2017.03.011.
[45] S. Yoshida et al., Acta Mater. 171 (2019) 201–215, https://doi.org/10.1016/j.actamat.2019.04.017.
[46] C. Keller, E. Hug, Mater. Lett. 62 (2008) 1718–1720, https://doi.org/10.1016/j.matlet.2007.09.069.
[47] M. Odnobokova, A. Belyakov, R. Kaibyshev, Metals 5 (2015) 656–668, https://doi.org/10.3390/met5020656.
[48] X. Li et al., J. Mater. Sci. Technol. 94 (2021) 264–274, https://doi.org/10.1016/j.jmst.2021.02.060.
[49] M. Schneider et al., Int. J. Plast. 124 (2020) 155–169, https://doi.org/10.1016/j.ijplas.2019.08.009.
[50] M.J. Yao et al., Acta Mater. 140 (2017) 258–273, https://doi.org/10.1016/j.actamat.2017.08.049.
[51] D. Kuhlmann-Wilsdorf, Mater. Sci. Eng. A 113 (1989) 1–41, https://doi.org/10.1016/0921-5093(89)90290-6.
[52] C. Lee et al., Nat. Commun. 12 (2021) 5474, https://doi.org/10.1038/s41467-021-25807-w.
[53] T. Ungár et al., J. Appl. Crystallogr. 32 (1999) 992–1002, https://doi.org/10.1107/S0021889899009334.
[54] G. Ribárik, B. Jóni, T. Ungár, Crystals 10 (2020) 623, https://doi.org/10.3390/cryst10070623.
[55] B. Jóni et al., Acta Mater. 61 (2013) 632–642, https://doi.org/10.1016/j.actamat.2012.10.008.
[56] C. Lee et al. eaaz4748, Sci. Adv. 6 (2020), https://doi.org/10.1126/sciadv.aaz4748.
[57] M.A. Meyers, O. Vöhringer, V.A. Lubarda, Acta Mater. 49 (2001) 4025–4039, https://doi.org/10.1016/S1359-6454(01)00300-7.
[58] Y.Z. Tian et al., Acta Mater. 110 (2016) 61–72, https://doi.org/10.1016/j.actamat.2016.03.015.
[59] B.C. De Cooman, Y. Estrin, S.K. Kim, Acta Mater. 142 (2018) 283–362, https://doi.org/10.1016/j.actamat.2017.06.046.
[60] S. Sato et al., Isij Int. 55 (2015) 1432–1438, https://doi.org/10.2355/isijinternational.55.1432.
[61] G. Kresse, J. Furthmüller, Comput. Mater. Sci. 6 (1996) 15–50, https://doi.org/10.1016/0927-0256(96)00008-0.
[62] G. Kresse, J. Hafner, Phys. Rev. B 47 (1993) 558, https://doi.org/10.1103/PhysRevB.47.558.
[63] J.P. Perdew, K. Burke, M. Ernzerhof, Phys. Rev. Lett. 77 (1996) 3865, https://doi.org/10.1103/PhysRevLett.77.3865.
[64] S. Zhao, G.M. Stocks, Y. Zhang, Acta Mater. 134 (2017) 334–345, https://doi.org/10.1016/j.actamat.2017.05.001.
[65] J. Zhang et al., Acta Mater. 219 (2021), https://doi.org/10.1016/j.actamat.2021.117238 117238.
[66] S. Zhao et al., npj Comput. Mater. 5 (2019) 13, https://doi.org/10.1038/s41524-019-0150-y.
[67] S. Plimpton, J. Comput. Phys. 117 (1995) 1–19, https://doi.org/10.1006/jcph.1995.1039.
[68] X. Zhou et al., J. Comput. Chem. 29 (2018) 2420–2431, https://doi.org/10.1002/jcc.25573.

[69] S. Zhao et al., Acta Mater. 219 (2019), https://doi.org/10.1016/j.actamat.2021.117233 117233.
[70] C. Varvenne et al., Phys. Rev. B 93 (2016), https://doi.org/10.1103/PhysRevB.93.104201 104201.
[71] D. Rodney, Acta Mater. 52 (2004) 607–614, https://doi.org/10.1016/j.actamat.2003.09.044.
[72] T. Shintani, Y. Murata, Acta Mater. 59 (2011) 4314–4322, https://doi.org/10.1016/j.actamat.2011.03.055.
[73] T. Ungár, A. Borbély, Appl. Phys. Lett. 69 (1996) 3173–3175, https://doi.org/10.1063/1.117951.